Gravitationally Induced Density Wake of a Circularly Orbiting Object As an Interpretative Framework of Ubiquitous Spirals and Arcs

Hyosun Kim[1]

ABSTRACT

An orbiting object in a gas rich environment creates a gravitational density wake containing information about the object and its orbit. Using linear perturbation theory, we analyze the observable properties of the gravitational wake due to the object circularly moving in a static homogeneous gaseous medium, in order to derive the Bondi accretion radius r_B, the orbital distance r_p, and the Mach number $\mathcal{M}_p$ of the object. Supersonic motion, producing a wake of spiral-onion shell structure, exhibits a single-armed Archimedes spiral and two-centered circular arcs with respect to the line of sight. The pitch angle, arm width, and spacing of the spiral pattern are entirely determined by the orbital distance r_p and Mach number $\mathcal{M}_p$ of the object. The arm-interarm density contrast is proportional to r_B, decreasing as a function of distance with a power index of -1. The background density distribution is globally changed from initially uniform to centrally concentrated. The vertical structure of the wake is manifested as circular arcs with the center at the object location. The angular extent of the arcs is determined by the Mach number $\mathcal{M}_p$ of the object motion. Diagnostic probes of nonlinear wakes such as a detached bow shock, an absence of the definite inner arm boundary, the presence of turbulent low density eddies, and elongated shapes of arcs are explained in the extension of the linear analysis. The density enhancement at the center is always r_B/r_p independent of the nonlinearity, suggesting that massive objects can substantially modify the background distribution.

Subject headings: hydrodynamics — ISM: general — waves

1.   INTRODUCTION

The gravitational interaction of orbiting objects with a background medium is fundamental in many astrophysical problems. Objects in gas-rich environments such as planets in protoplanetary disks, young stars in natal molecular clouds, substellar mass objects in stellar winds, compact objects orbiting around supermassive black holes, and supermassive black hole binaries in colliding galaxies are subject to the gravitational interaction with background gas. The orbiting object

---
[1]Academia Sinica Institute of Astronomy and Astrophysics, P.O. Box 23-141, Taipei 10617, Taiwan; hkim@asiaa.sinica.edu.tw

naturally generates a gravitational density wake in its environment, inevitably followed by the reaction of the induced wake as dynamical friction.

A recent series of studies on the gaseous dynamical friction is devoted to understand the orbital evolution of the object in rectilinear motion (Ostriker 1999; Sánchez-Salcedo & Brandenburg 1999; Kim & Kim 2009; Namouni 2010, 2011) and in circular motion (Sánchez-Salcedo & Brandenburg 2001; Kim & Kim 2007; Kim et al. 2008; Kim 2010). These theoretical and numerical works have covered the effects of binarity, nonlinearity, acceleration, and background stratification. Albeit all these factors give rise to appreciable effects, the density wake and the dynamical friction force are primarily characterized by the accretional and orbital properties of the object described by the linear perturbation analyses in Ostriker (1999) and Kim & Kim (2007, hereafter KK07).

Given the importance of the gravitational drag, these linear analyses have been applied to various astrophysical aspects such as the orbital decay of planets around giant stars (Schröder & Connon Smith 2008; Villaver & Livio 2009), the primordial mass segregation in massive star forming regions (Garay et al. 2010; Chavarría et al. 2010), the binary hardening in parent gaseous disk (Baruteau et al. 2011), the deceleration of galaxies as the heating sources of intracluster medium against the cooling flows (El-Zant et al. 2004; Kim et al. 2005; Kim 2007; Conroy & Ostriker 2008), and the coalescence of supermassive black holes in gas-rich mergers of galaxies (Escala et al. 2004, 2005; Dotti et al. 2006, 2007; Mayer et al. 2007). These linear analyses have been extended to the relativistic case (Barausse 2007) for extreme mass-ratio inspirals in the vicinity of supermassive black holes. In particular, Barausse & Rezzolla (2008) found an important difference in the inclination angle of the orbits between the dynamical friction and the radiation reaction possibly detectable by Laser Interferometer Space Antenna (LISA).

Also important are the morphological and kinematic features of the density wake per se, as they can be directly observed by means of X-rays in shocked regions, molecular line emissions, dust continuum emissions, and in dust scattered light. Furlanetto & Loeb (2002) raised the possibility that the nature of dark matter can be examined by detailed X-ray observations of wakes due to the motion of galaxies in the intracluster medium, exhibiting distinguishable pictures between the standard collisionless cold dark matter and the collisional (fluid) dark matter. Sánchez-Salcedo (2009) furthermore proposed that the morphology of a galactic wake in X-ray emission differs in purely baryonic Modified Newtonian Dynamics (MOND) from the case of Newtonian gravity with dark matter. These authors only inspected the local attributes of the gravitational density wakes using Ostriker's (1999) formulae for the cases of the perturbing object in rectilinear motion.

However, many observable objects have fairly short orbital periods compared to the dispersion timescale of the background gaseous matter, leading to global shaping of the induced wakes. KK07 showed that the curvilinear orbit modifies not only the curvature of the wake but transformes the overall structure entirely because of the memory effect[1]. One application of the large scale wakes

---

[1] Memory effect (or battery effect) originally refers, only in nickel cadmium rechargeable batteries, to the symptom

is to a case that planets or brown dwarfs lie in cool giant envelopes, whose wakes are possibly observable at large distances from their bright parent stars. Future high sensitivity/resolution observations of these wakes can provide evidence of the unseen substellar mass objects, further allowing us to derive their orbital properties (Kim & Taam 2011 in prep.; for a brief introduction see Kim & Taam 2011).

Although KK07 calculated the density wake, they primarily focused on the dynamical friction force that affects the initially circular orbit and the description of the general wake feature was somewhat superficial. A more detailed understanding of the wake characteristics is necessary in order to provide an interpretative framework for both further theoretical works under more complicated situations and future observations to detect the gravitational wakes of hidden objects. In this paper, we extend the semianalytic work of KK07 highlighting the observable quantities, and determine the detailed structure and kinematics of the gravitational wake due to an object in circular motion. Particularly, we study the density structure in great detail based on an analytic linear analysis, which also helps to understand aspects of the simulated density wake in a nonlinear regime. We provide the density contrast of the wake as a function of the object mass, orbital radius, orbital speed, and the background sound speed, providing a way to obtain the information of unseen orbiting object from the observation of the wake at a large distance.

This paper is organized as follows. In §2 we review the derivation and findings in previous works as the starting point of this investigation. In §3 we present the nature of linear wake as revealed in the shape (§3.1), the density enhancement (§3.2), and the velocity distribution (§3.3), provided that the weak gravitational influence is thoroughly described in the linear perturbation analysis. In §4, based on the linear wake properties, we suggest a new explanation for nonlinear effects manifested on the wake when the perturbation in discontinuity is saturated. In §5 we summarize the newly found properties of the gravitationally induced wake of a circularly orbiting object in a static uniform gaseous medium, and briefly consider applications to a few astronomical objects.

2. BACKGROUND REVIEW

Starting from the basic equations of hydrodynamics with an external time-dependent gravitational potential Φ_p but excluding self-gravity of the gaseous medium, one can obtain a linearized three dimensional wave equation for the density enhancement $\alpha = \delta\rho/\rho$ under the assumption of a small perturbation ($\alpha \ll 1$),

$$\nabla^2 \alpha - \frac{1}{c_s^2} \frac{\partial^2 \alpha}{\partial t^2} = -\frac{1}{c_s^2} \nabla^2 \Phi_p. \tag{1}$$

of losing their maximum energy capacity after being repeatedly recharged to partially discharged states. We apply this term here for the wake repetitively perturbed by the revolving object over the former perturbations remained, resulting in a loss of density contrast, as we will mention at the end of this paper.

Here, $c_{\rm s} = (\gamma p/\rho)^{1/2}$ is the sound speed of unperturbed gas with density ρ, thermal pressure p, and adiabatic index γ in general. Ostriker (1999) applied it to the situation that the perturbing object is in rectilinear motion through an infinite homogeneous gaseous medium, utilizing the retarded Green's function technique (Jackson 1975) based on the Fourier transform (see also Just & Kegel 1990). A purely analytic solution for the density enhancement was derived, which can be expressed as

$$\alpha = \frac{r_B}{\left(d_\parallel^2 + d_\perp^2(1 - \mathcal{M}_p^2)\right)^{1/2}} \sum_{d_\parallel'} \mathcal{H}\left(V_p t - d_\parallel'\right) \tag{2}$$

in the axisymmetric coordinates $(d_\parallel, d_\perp)$ with the origin at the perturbing object, $d_\parallel$ along the tail (i.e., in the opposite direction of the orbital motion) and $d_\perp$ in the orthogonal direction. Here, we define the most important parameters in this paper, r_B and $\mathcal{M}_p$, as the Bondi accretion radius and the orbital Mach number of the object, respectively. In the summation of the Heaviside step functions $\mathcal{H}$, the primed distance $d_\parallel'$ denotes the original position of the gravitational perturbation, initiated by the object and currently arriving at the observing point $(d_\parallel, d_\perp)$. Thus, the integrand means that the perturbation sources should be on the trace of the object, inevitably not able to be further than the initial position of the object, $V_p t \geq d_\parallel'$. The summation of only the step functions indicates the exactly same contributions from the individual perturbations gathered at a time. Accordingly, it can be substituted simply by the number of perturbations at the point, $\mathcal{N} = \sum_{d_\parallel'} \mathcal{H}\left(V_p t - d_\parallel'\right)$, which divides the space into three regions showing discontinuous density and velocity distributions: $\mathcal{N} = 2$, 1, and 0 in the cone region, in the ice cream region, and outside of these two regions (as following the author's original nomenclature). These three regions are separated by the sharp edge of a Mach cone and the modest edge of a sonic sphere about the initial position of the object. As the orbital Mach number $\mathcal{M}_p$ decreases, the apex of the Mach cone attached to the object approaches to, and finally disappears in, the sonic sphere with the transition occurring at the sonic speed ($\mathcal{M}_p = 1$), eliminating the shock front from the density wake.

Using the same retarded Green's function technique, KK07 applied the three dimensional wave equation (eq. [1]) to the linear wake induced by a circularly orbiting object at distance r_p from the system center in a static uniform gaseous background. The resulting density enhancement is given as

$$\alpha = \frac{r_B}{r_p} \sum_{\varphi'} \frac{\mathcal{H}\left(V_p t/r_p - \varphi'\right)}{\left|\mathcal{M}_p^{-1}\varphi' - \mathcal{M}_p(r/r_p)\sin(\varphi' - \varphi)\right|} \tag{3}$$

in cylindrical coordinates[2] (r, φ, z) with the equatorial plane aligned to the orbital plane of the perturbing object. All the possible perturbations must be launched from the object passing through the locations $(r_p, \varphi', 0)$, where φ' satisfies the condition,

$$\mathcal{M}_p^{-1}\varphi' = \left(1 + (r/r_p)^2 + (z/r_p)^2 - 2(r/r_p)\cos(\varphi' - \varphi)\right)^{1/2}. \tag{4}$$

---

[2] φ is the angular distance from the object in the opposite direction of the orbital motion, tracing the induced wake tail, i.e., the perturbing object has moved from $V_p t/r_p$ (>0) to 0. This is corresponding to $-s$ in the notation of KK07.

This relation describes that the individual perturbation propagates from the launching point $(r_p, \varphi', 0)$ to the observing point (r, φ, z) as a sound wave during the time that the perturbing object travels the angular distance $r_p\varphi'$ along the orbit with the speed $\mathcal{M}_p$. In the case of curvilinear motion, the summation is not only restricted to the step function, implying different contributions from the different elements of the perturbations. This diversity of contributions is the primary reason of the complications arising in a density wake of the circularly orbiting object.

KK07 accurately calculated the wake density in equation (3) by computing the positions of perturbation origins in the nonlinear equation (4) using root-finding algorithms based on either Newton-Raphson or bisection iterations. Their accurate numerical values, however, do not provide deep physical insight for the global features of the induced density wake, which are useful to probe the orbital properties of the perturbing object. In this paper, we revisit KK07's work on the linear density wake of a circularly orbiting object by modifying their analytic formulae and by inspecting the global distributions of the calculated density enhancement and velocity fields, if necessary, in comparison with the linear trajectory counterparts. In addition, we have performed high resolution three dimensional hydrodynamical simulations using an adaptive mesh refinement code, FLASH (Fryxell et al. 2000), to investigate the response of a gaseous medium to the influence of an extended object, characterized by a gravitational softening radius r_s in the range of 0.01–0.1 r_p (alternatively, 0.1–25 r_B) for $\mathcal{M}_p = 0.2$–10. This parameter space includes the nonlinear regime showing different behaviors of the wake from the ones in the linear analysis (see also Kim & Kim 2009; Kim 2010). All the simulations treat only a pseudo-isothermal gas with $\gamma = 1.00001$ in the FLASH code, providing a constant sound speed c_s in the entire computational domain.

3. LINEAR WAKE

3.1. Morphology

An object orbiting with a subsonic speed ($\mathcal{M}_p < 1$) creates a smoothly distributed wake without a shock, showing a gradual decrease of density along the distance from the perturbing object. The isodensity surfaces of this subsonic wake have the shapes of oblate spheroids with ellipticity $e = \mathcal{M}_p$ near the perturbing object (see Appendix A of KK07 for derivation), gradually twisted in a trailing fashion with the low-density outermost shells tending toward comma shapes. The morphology of a subsonic wake is simple and easily understood since the wake receives only one sonic perturbation everywhere, contrary to the supersonic wakes ($\mathcal{M}_p > 1$) investigated in depth in this section.

The wake induced by a circularly orbiting object with supersonic speed has a spiral-onion shell structure in three dimensional space, having distinct boundaries for the high density region and the lower density inter-structure regions. The density contrast is primarily caused by the piling up of the delayed gravitational perturbations inside the high density structure. Equation (4) gives the positions of the origins, φ', for the perturbations reaching the observing point (r, φ, z) at time

t. After some algebra from equation (4), KK07 showed that the high density structure possesses $\mathcal{N} = 2n + 1$ perturbations, where n is an integer number depending on the orbital Mach number such as 1 ($\mathcal{N} = 3$) at $\mathcal{M}_p \sim 1 - 4.6$, 2 ($\mathcal{N} = 5$) at $\mathcal{M}_p \sim 4.6 - 7.8$, 3 ($\mathcal{N} = 7$) at $\mathcal{M}_p \sim 7.8 - 10.9$, and so on (see Appendix B of KK07 for a more detailed discussion). For comparison, in subsonic cases ($\mathcal{M}_p < 1$) the wake receives one perturbation ($\mathcal{N} = 1$) everywhere, corresponding to $n = 0$.

Extending the analysis in Appendix B of KK07, in which the number of perturbations of the arm structure in the orbital plane is obtained, we derive a purely analytic formula to describe the exact shape of the enhanced density structure in three dimensional space. The details of the derivation are omitted but the essence is to use the property at the boundaries, where the number of perturbations changes so that the curve on the right hand side of equation (4) has the same slope as the line on the left hand side. We derive an expression for the shape of the enhanced density structure given by

$$\cos\left(\left|(X^2 - 1)^{1/2} \mp (Y^2 - 1)^{1/2}\right| - \varphi\right) = \frac{1 \pm (X^2 - 1)^{1/2}(Y^2 - 1)^{1/2}}{XY} \tag{5}$$

for the outer (*upper sign*) and inner (*lower sign*) boundaries, where X and Y are defined as $X = \mathcal{M}_p(d_+ + d_-)/2$ and $Y = \mathcal{M}_p(d_+ - d_-)/2$. Here, the normalized distances $d_- = \left((r - r_p)^2 + z^2\right)^{1/2}/r_p$ from the perturbing object and $d_+ = \left((r + r_p)^2 + z^2\right)^{1/2}/r_p$ from the mirror point about the system center. The solutions of these formulae determine the boundaries of the high density region, revealed in Figure 1a–b as a single-armed spiral in the orbital plane ($z = 0$) and arcs in a meridional plane ($\varphi = 0$).

3.1.1. Spiral

Shaping a spiral arm having a constant width is physically not so trivial for the density wake in a uniform background. Because of the gas pressure, the gaseous matter accumulated behind the object tends to disperse with the sound speed in a static uniform background. Thus, the excess density region should form an extending tail similarly to the Mach cone shape in the linear trajectory counterpart, unless the background density configuration is changed. As we will show in §3.2.1, the initially uniform background transforms the distribution into a hydrodynamic equilibrium about the system center. As the result of the centrally concentrated background, the inner part of the spiral does not propagate inward but outward, following its outer part.

In this section, we construct an explicit form of the spiral shape, which is important in order to derive the pitch angle, the arm width, and the spacing of the spiral pattern, relevant to the object orbital parameters. Equation (5) at $z = 0$ yields the polar equations for the boundaries of the spiral arm in the orbital plane (see also eq. [B2] in KK07),

$$\varphi = \left|\left(\mathcal{M}_p^2(r/r_p)^2 - 1\right)^{1/2} \mp \left(\mathcal{M}_p^2 - 1\right)^{1/2}\right| - \cos^{-1}\left(\frac{1 \pm \left(\mathcal{M}_p^2 - 1\right)^{1/2}\left(\mathcal{M}_p^2(r/r_p)^2 - 1\right)^{1/2}}{\mathcal{M}_p^2(r/r_p)}\right) \quad \text{at} \ \ z = 0, \tag{6}$$

in which the upper and lower signs are for the outer and inner boundaries, respectively. The outer boundary of the arm, originated from the Mach cone in Ostriker (1999), lies not only outside the orbit $(r/r_p \geq 1)$ but it also extends to $r/r_p = \mathcal{M}_p^{-1}$ (see Fig. 1 in KK07). At this innermost point of the outer boundary, the sonic sphere due to the influence of the gravitational perturbation from the object at the initial location starts to overlap with the curved Mach cone tailing the object, forming the inner boundary of the spiral arm.

In order to see the global features of the wake in the orbital plane, we differentiate the complicated forms (eq. [6]) following the exact shapes. Using the angle transformation formulae for cosine, it is reduced to

$$\frac{d(r/r_p)}{d\varphi} = \frac{r/r_p}{\left(\mathcal{M}_p^2(r/r_p)^2 - 1\right)^{1/2}} \tag{7}$$

for both outer and inner arm boundaries in the orbital plane, except for a small part of the outer boundary inside the orbit $(\mathcal{M}_p^{-1} < r/r_p < 1)$ having the opposite sign. We define an angle Θ as its tangent value, $\tan\Theta$, corresponding to equation (7), which leads to the alternative form

$$\sin\Theta = \frac{r/r_p}{\left((\mathcal{M}_p^2 + 1)(r/r_p)^2 - 1\right)^{1/2}}, \tag{8}$$

resulting in the familiar result $\Theta = \sin^{-1}\mathcal{M}_p^{-1}$ at the object position $r/r_p = 1$ as the half-opening angle of the curved Mach cone (KK07; see also Ostriker 1999). This angle Θ decreases along the distance r/r_p as seen in equations (7) and (8), but it converges very quickly to $\Theta = \tan^{-1}\mathcal{M}_p^{-1}$, showing a small deviation of $\leq 1°$ at $r/r_p \geq 2$ for $\mathcal{M}_p \geq 2$ ($r/r_p \geq 4$ for $\mathcal{M}_p = 1$). This quasi-constancy of Θ suggests that the density wake in a static gaseous medium indeed approximates an Archimedes spiral, satisfying $r/r_p = \varphi\mathcal{M}_p^{-1} + C$ where the constant C differs between the inner and outer boundaries of the high density arm region. Figure 1a displays the density enhancement in the orbital plane $(z = 0)$ of the perturbing object, and exhibits a high density region enclosed by two Archimedes spirals shown in dashed $(C = 1)$ and dotted $(C = -0.7$ for $\mathcal{M}_p = 10)$ lines. The constant C's are calculated at $r/r_p = 1$ using equation (6); the value for the inner boundary changes with $\mathcal{M}_p$, while it is unity for the outer boundary.

3.1.2. Arcs

An investigation of the wake shape in a meridional plane is needed to provide an interpretative framework for edge-on observations. Compared to the asymmetric spiral pattern seen in the face-on line of sight, this arc pattern is not properly spotlighted and hence not analyzed well. In this section, we show the purely analytic solution for the arc shape of the gravitational wake, and use a geometrical approach to fully understand the wake shape relevant to the object properties.

A trivial solution of equation (5) is both $X = 1$ and $Y = 1$ in the meridional plane wherein the perturbing object lies $(\varphi = 0)$, which indicates the (vertically) highest intersecting points between

the outer and inner boundaries, i.e., the extension limit of the intensively perturbed region. $X = 1$ and $Y = 1$ stand for an ellipse and a hyperbola, by definition, with the common foci at the location of the perturber and the mirror point about the orbital axis. However, both $X = 1$ and $Y = 1$ actually correspond to the same formula for a hyperbola

$$\mathcal{M}_p^2 (r/r_p)^2 - \frac{\mathcal{M}_p^2}{\mathcal{M}_p^2 - 1}(z/r_p)^2 = 1, \tag{9}$$

since we only consider the shape of a wake induced by a supersonic perturber ($\mathcal{M}_p > 1$). The vertex of the hyperbola, $r/r_p = \mathcal{M}_p^{-1}$, corresponds to the distance of the junction between the outer and inner arm boundaries in the orbital plane. The extension limit of the high density arcs in the vertical direction is simplified to the asymptotes of the hyperbola,

$$z = \pm (\mathcal{M}_p^2 - 1)^{1/2} r, \tag{10}$$

which are overlaid by black lines in Figure 1b. This indicates that the angular size of the arcs is $2 \tan^{-1}(\mathcal{M}_p^2 - 1)^{1/2}$, further extended with higher orbital Mach number. This vertical stretch, however, does not depend very strongly on $\mathcal{M}_p$ except for near unity (i.e., $60°- 90°$ for $\mathcal{M}_p \geq 2$).

In Figure 1b individual segments of the boundaries, satisfying equation (5), appear to be circular arcs about the centers at either the object position or the mirror point. In the plane of the object ($\varphi = 0$; $x > 0$), the arcs extended from the outer boundaries of the spiral arm in Figure 1a (i.e., $x/r_p = 1$, $1 + 2\pi\mathcal{M}_p^{-1}$, $1 + 4\pi\mathcal{M}_p^{-1}$, $1 + 6\pi\mathcal{M}_p^{-1}$, $1 + 8\pi\mathcal{M}_p^{-1}$, and $1 + 10\pi\mathcal{M}_p^{-1}$ at $z/r_p = 0$) center around the perturbing object at $(x, z)/r_p = (1, 0)$. These concentric arcs have endpoints on the hyperbola defined in equation (9) (or, the asymptotes in eq. [10]), except for the point (not visible) at the perturber position and the curve passing through $(x, z)/r_p = (1 + 2\pi\mathcal{M}_p^{-1}, 0)$, which completes its full circle. The inner x-intercept of this circle at $x/r_p = 1 - 2\pi\mathcal{M}_p^{-1}$ actually corresponds to the inner edge of the curved Mach cone, which is considered as a part of the outer arm boundary (see §3.1.1) and, here, this is clarified. On the other hand, the arcs crossing the inner arm boundaries on this side ($x > 0$) have the center at the mirror point $(x, z)/r_p = (-1, 0)$, resulting in larger radii compared to the radii of the outer counterparts. The outer boundaries on the opposite side ($x < 0$), i.e., the arcs having intercepts at $x/r_p = -1 - \pi\mathcal{M}_p^{-1}$, $-1 - 3\pi\mathcal{M}_p^{-1}$, $-1 - 5\pi\mathcal{M}_p^{-1}$, $-1 - 7\pi\mathcal{M}_p^{-1}$, and $-1 - 9\pi\mathcal{M}_p^{-1}$, are concentric about the mirror point of the object, $(x, z)/r_p = (-1, 0)$. On this side ($x < 0$), instead, the center of the inner boundaries is at the object position, $(x, z)/r_p = (1, 0)$.

The inner and outer boundaries, in fact, constitute the same circles, which is better visualized in Figure 2 for the number of perturbations. Particularly, the largest sphere about $(x, y, z)/r_p = (1, 0, 0)$ limits the region already in a steady state, receiving 1, 3, 5, and 7 perturbations in different localities. The arcs (or circles) in Figure 2b are formalized by equation (4)[3] with the sources at φ' of π-multiples in the plane of $\varphi = 0$. The perturbation launched every time the object returns

---

[3] Eq. (5) gives the same results. Since $|(X^2 - 1)^{1/2} \mp (Y^2 - 1)^{1/2}|$ in this equation is originated from φ' in eq. (4),

back to the original position (φ' being a multiple of 2π) propagates as a sound wave leaving the vestige on the spherical shell with the radius of multiple of $2\pi\mathcal{M}_p^{-1}$; the perturbation generated half an orbit (π in angular phase) later is marked on the sphere, smaller by $\pi\mathcal{M}_p^{-1}$, with the center at the mirror point in the same meridional plane. And by extension, the spiral in the orbital plane (Fig. 2a) emerges as an aftermath of the phase difference of the perturbation source.

3.2. Density Enhancement

The density enhancement, α, in the pattern follows a complicated rule because of the accumulation of gravitational perturbations launched from the object at different positions on the curvilinear orbit. This complication is particularly caused by the different contributions of the respective perturbations, unlike the case when the object is in a straight-line trajectory. The density enhancement profiles are displayed in Figure 1c as a function of radial distance in various directions along the spiral arm (the lines in red, yellow, green, and blue colors) and along the orbital axis (the cyan line), in which all the curves appear well located within the black lines (see below). The profiles in the orbital plane reveal the highest density peaks at the object orbit, $r/r_p = 1$, and the peak values decrease with distance from the orbit. The minimum density enhancement in azimuthal directions, i.e., the baseline of the group of profiles, gradually decreases following the bottom dashed line (up to $r/r_p = 0.4$) starting from $\alpha = r_B/r_p$ at the orbital center. At $r/r_p = 0.4$, however, the baseline jumps to, and follows, another dashed line, and another jump occurs at $r/r_p = 0.75$. In this example case of $\mathcal{M}_p = 10$, the baseline moves its paths among the dashed lines through three steps before reaching the orbital radius. Beyond the orbital radius, it follows the third dashed line from bottom until it abruptly drops at $r/r_p \sim 2.5$ apart from the path. This last drop of minimum density enhancement coincides with the sudden disappearance of the inner arm boundary, which is related to the orbital evolution time of the object. Using the spiral functional forms deduced in §3.1.1, it is shown that the outer and inner arm boundaries reach $r/r_p = 4.1$ and 2.4, respectively, at the moment that the perturber completes 5 orbits (i.e., $\varphi = 10\pi$). The inner arm boundary lags behind by 2.7-turn since it starts from $(r/r_p, \varphi) = (\mathcal{M}_p^{-1}, 1 + 0.7\mathcal{M}_p)$, deeper inside than the starting point of the outer boundary at $(r/r_p, \varphi) = (1, 0)$.

---

eq. (5) is equivalent to $(X^2 + Y^2 - 2XY\cos(\varphi' - \varphi))^{1/2} = \varphi'$. In the meridional plane of $\varphi = 0$, the gravitational perturbations from the object located, in the past, at $\varphi' = 2\pi \times 0$ (*current*), 1, 2, 3, 4, and 5 (*initial*) form the arcs as the segments of circles, $d_- = (X - Y)\mathcal{M}_p^{-1} = 2\pi\mathcal{M}_p^{-1} \times 0$, 1, 2, 3, 4, and 5. Similarly, $\varphi' = \pi \times 1$, 3, 5, 7, and 9 correspond to the concentric arcs on $d_+ = (X + Y)\mathcal{M}_p^{-1} = \pi\mathcal{M}_p^{-1} \times 1$, 3, 5, 7, and 9.

3.2.1.   Interarm Region

Equations (3)–(4) indicate that the minimum of density enhancement in the azimuthal direction satisfies[4]

$$\alpha_{\min} = \frac{r_B}{(r^2 + z^2 + r_p^2)^{1/2} + r\mathcal{M}_p}.$$ (11)

This is plotted in Figure 1c by the bottom dashed line, outlining the interarm density enhancement for all directions. The incremental steps, observed above, follow the dashed lines exhibiting $\alpha = \alpha_{\min}(r, z = 0) \times 1, 4, 7, \cdots, 1 + 3n$, where $n = (\mathcal{N} - 1)/2$ is 0, 1, 2, etc. depending on the orbital Mach number $\mathcal{M}_p$ (for n see §3.1, originated by eq. [B3] in KK07).

To examine the dependence of the minimum density enhancement on $\mathcal{M}_p$ (technically, n), we compare the α-profiles for $\mathcal{M}_p$ of 0.8 ($n = 0$), 2.0 ($n = 1$), 4.5 ($n = 1$), and 5.0 ($n = 2$) in Figure 3, having $n + 1$ dashed lines in each panel. Unlike the subsonic case ($n = 0$) having smooth α-profiles above $\alpha_{\min}$ in Figure 3a, the supersonic cases ($n \geq 1$) in Figure 3b-d show arm structures with sharp boundaries of higher density than in the middle of the arm. In Figure 3b for $\mathcal{M}_p = 2$ ($n = 1$), the interarm density is still represented by $\alpha_{\min}$ (*lower dashed*) and the local minimum inside the arm is higher than $4\alpha_{\min}$ (*upper dashed*). Increasing $\mathcal{M}_p$ (up to 4.6) increases the arm width with a corresponding decrease in interarm extent (see Fig. 3c). The minimum arm densities concurrently approach $4\alpha_{\min}$. At the critical Mach number $\mathcal{M}_p = 4.6$, the outer boundary of the arm meets with the inner boundary of the arm one turn ahead, leaving no gap between arms. Because of this overlap (outside the orbit), the colored lines in Figure 3d for $\mathcal{M}_p$ beyond 4.6 no longer exist on the bottom dashed line ($\alpha = \alpha_{\min}$). Instead, the minimum density is now given by the value of $\alpha = 4\alpha_{\min}$, characterized as the local density minimum within the (infinitely) broad arm, above which a new narrow arm forms. The new arm possesses an increased number $\mathcal{N}$ of perturbations, changing n from 1 to 2, because this arm is basically the overlapping region. Increasing $\mathcal{M}_p$ above 4.6 repeats the same broadening of the new arm until $\mathcal{M}_p$ reaches another critical Mach number, 7.8. Above this critical Mach number, an overlapping event causes another jump of the minimum density to $(1 + 3(n - 1))\alpha_{\min}$ with the increased n (≥ 1, in general), and leads to the density of the newly formed arm above $(1 + 3n)\alpha_{\min}$.

As shown in Figure 1b, the density structure at high latitudes ($|z| > 0$) is more complicated because of the partial overlaps of overdense areas closed by arcs with different radii. The overdense regions induced by a slower object ($1 < \mathcal{M}_p < 4.6$) are composed of simple crescent-shapes without overlap. However, once overlapped ($\mathcal{M}_p \geq 4.6$), the regions of interest exhibit enhanced densities because they swallow the perturbations of each crescent-shaped structures. For instance, the case

---

[4] Strictly, eqs. (3)–(4) imply the minimum value of density enhancement in the central part $r/r_p < 2\mathcal{M}_p^{-2}$ is better represented by $\alpha \simeq r_B / \left((r + r_p)^2 + z^2\right)^{1/2}$ than $\alpha_{\min}$ defined in eq. (11). This is simply seen in an extreme case of $\mathcal{M}_p = 0$ so that $2\mathcal{M}_p^{-2}$ goes to infinity; its density wake in hydrostatic equilibrium about the static perturber at $(r, \varphi, z) = (r_p, 0, 0)$ shows the density enhancement $\alpha = \exp(r_B/d) - 1 \approx r_B/d$ (when $r_B/d \ll 2$) at the distance $d = (r^2 + z^2 + r_p^2 - 2rr_p \cos\varphi)^{1/2}$ from the perturber, which has the minimum value at $\varphi = \pi$.

in Figure 1 ($\mathcal{M}_p = 10$) experiences 3 steps of density enhancement (corresponding to the number of perturbations $\mathcal{N} = 7$) within the discernible spiral arm in the orbital plane. But the number of perturbations decreases at high latitude where the overlapping events are reduced (see also Fig. 2b). Eventually above the extension limit (Eq. [9]), the gas flow experiences only one perturbation so that the density enhancement has the value of $\alpha_{\min}(r, z)$ (see cyan line in Figure 1c along the dotted line, $\alpha = \alpha_{\min}(r = 0, z)$).

3.2.2. Arm Region

In order to understand the distribution of the peak densities along distance, it is preferable to refer to the simpler case of the perturbing object moving on a linear trajectory, whose respective perturbations equally contribute to the density enhancement of the induced wake. Ostriker's formula for the linear motion of a perturber (eq. [2]) has roughly an anticorrelation with respect to the distance from the perturbing object with the amplitude of $r_B |\mathcal{M}_p^2 - 1|^{-1/2}$ per each contribution. Modifying Ostriker's formula, for circular orbit cases we hypothesize a density enhancement due to one perturbation,

$$\alpha_1 = \frac{r_B}{|r - r_p|} \frac{1}{|\mathcal{M}_p^2 - 1|^{1/2}} \tag{12}$$

in the orbital plane. However, in reality, the circular motion modifies the density enhancement from a simple collection of α_1 by the number of perturbations. Particularly, gas pressure at the central region prevents the propagation of Mach waves, forming instead an equilibrium state with the central value $\alpha = r_B/r_p$. A rough guess of α_1 can be used in an empirical formula for the peak density enhancement in the spiral arm pattern,

$$\alpha \approx \alpha_1 + 2\mathcal{N}\alpha_{\min}, \tag{13}$$

which shows fairly good fits in Figures 1c and 3 (see black solid curve), except at the exact locations of the arm boundaries where infinite values are introduced by the point mass perturber (see below).

3.2.3. Effect of Object Size

Although, mathematically, the perturbation from a point mass causes infinite density at the exact locations of arm boundaries, it is limited to the immediate vicinity of the arm boundaries, detectable only at extremely high angular resolution. For an extended object, the very sharp density peaks smear out depending on the size of the object, r_s, but the peak densities change significantly only within a distance of the order of r_s from the boundaries (see Fig. 6b of Kim 2010). In order to see the effects of the object size on the global structure of the density wake, we compare the density enhancement α in Figures 1, 4, and 5 for the cases of $r_s/r_p = 0$, 0.01, and 0.1, respectively, where the object size r_s is defined as the gravitational softening radius of a Plummer-type object. From Figures 1a–b, 4a–b, and 5a–b, one finds that the sharpness at boundaries are

reduced with the softened gravitational potential, while there are negligible changes in the global shape and morphology of the wake. The profiles of α along the spiral pattern in Figure 4c show the smoothing of arm boundaries compared to Figure 1c, chiefly by reducing the peak densities. Figure 5c indicates, however, that the minimum value of α is also changed in the case of the further extended object with size r_s comparable to or larger than half of the interarm spacing for the point mass counterpart, reducing the contrast between arm and interarm densities.

3.3. Velocity

In Figure 6 zooming in on a high density structure of the wake, the initially static medium is revealed to attain an approximately spherical velocity field. In order to understand the velocity features of the wakes for circularly orbiting objects, we first inspect the linear trajectory counterparts formulated in Kim & Kim's (2009) equations (A19)–(A20). From their formulae for the velocity components $V_\parallel$ and $V_\perp$ parallel and perpendicular to the object motion, respectively, it is straightforward to show that in the linear Mach cone (half-opening angle of $\Theta_M = \sin^{-1}\mathcal{M}_p^{-1}$) (1) the perturbed gas flows toward the edge of the cone perpendicularly, i.e., the fluid angle is $\tan^{-1}(|V_\perp/V_\parallel|) \simeq 90° - \Theta_M$ in the vicinity of the boundary, deflected from $0°$ heading for the object behind it (see also Fig. 1 in Sánchez-Salcedo & Brandenburg 1999 and Fig. 8 in Namouni 2011); and (2) the fluid speed in terms of Mach number approaches the value of the density enhancement ($\mathcal{M} \sim \alpha$) close to the boundaries but decreases to $\mathcal{M} = r_B\,(\mathcal{M}_p\,d)^{-1}$ along the line of the object motion at distance d from the object (see also Fig. 1 in Kim & Kim 2009). Overall, the fluid in a Mach cone has the maximum velocity near, and toward, the boundaries, although it deflects in angle for considerably slower fluid parts giving smaller contribution on average.

In the extension of this tendency of the flow to aggregate perpendicularly to the shocked boundary, it can be understood that the velocity vectors in Figure 6 appear to be spherical especially around the tightly wound spiral- and circular arc-shaped structures. The spiral boundaries in the orbital plane have a small pitch angle[5] of $\tan^{-1}(\mathcal{M}_p\,r/r_p)^{-1}$ (see §3.1.1) $\leq 10°$ at $r/r_p \leq 3$ for $\mathcal{M}_p \geq 2$ up to at $r/r_p \leq 6$ for the extreme case of $\mathcal{M}_p = 1$, making the velocity vectors further spherical at larger distances even in the marginally supersonic case. The velocity fields normal to the circular arcs in the meridional planes are obviously spherical at large distances, notwithstanding that the centers of the arcs are technically not at the system center but at $(r, z)/r_p = (\pm 1, 0)$ (§3.1.2). As implied by the above inspection of the velocity field in a Mach cone, the flow directions inside the high density structure are not normal to the boundary shapes. However, the magnitudes of speeds are negligible compared to the maximum speeds around the boundaries, $\mathcal{M} = r_B\mathcal{M}_p^{-1}|r - r_p|^{-1} \times 2\,(r_s/r_p)^{-1/3}$ in Mach number, which is empirically found in the range of $\mathcal{M}_p = 1$–10 and $r_s/r_p = 0.01$–0.1 with $r_B/r_p = 0.01$. It also deserves mentioning that the flow aggregates toward the outer boundary, while it tends to diverge from the inner boundary originated from the behavior

---

[5] The pitch angle of a spiral is defined by $\tan^{-1}\left(\frac{1}{r}\frac{dr}{d\varphi}\right)$, which at $r = r_p$ corresponds to Θ defined in §3.1.1.

of flow on a sonic sphere.

4. NONLINEAR WAKE

The density enhancement of a wake is related to r_B/r_p. As this value increases, for a fixed $\mathcal{M}_p$, the arm density increases and finally becomes saturated, showing unexpected behaviors. In previous numerical simulations (Kim & Kim 2009; Kim 2010), the nonlinear features such as a detached bow shock, turbulence, a disappearance of the inner arm boundary, and an increase of background density were exhibited without a clear explanation. In this section, we describe the nonlinear features of the wake based on the linear analysis in the previous section, emphasizing a new explanation for the detached bow shock as a phase shift of the inner boundary (defined for the corresponding linear wake). With this new explanation, we show that the nonlinear features are natural consequences, thus understandable in terms of an extension of the properties of linear wakes.

In Figure 7, we show the vertical structures of wake density and velocity field for $\mathcal{M}_p = 5$, just above a critical Mach number 4.6, causing the shallow overlaps between the crescent-shaped overdense regions predicted in the linear analysis. The wake shape in Figure 7a (for $r_B/r_p = 0.01$) is well explained by the linear prediction in §3.1.2 (dashed and dotted lines), except for the broadening of the edges to form high density belts of width $2r_s$. In addition, the inner boundaries of the crescents (dotted lines) are enlarged by r_s in radius compared to the prediction, since they form when the sonic sphere encounters the curved Mach cone broadened by r_s. The velocity field in Figure 7a shows the flow from the inner dotted arcs to the outer dashed arcs. These dotted and dashed lines are duplicated in Figure 7b as a reference to the flow pattern in the linear wake.

The wake in Figure 7b is induced by a 100 times stronger gravitational potential than in Figure 7a. This nonlinear wake preserves the density discontinuities at the outermost edges of the crescent shapes in the linear counterpart (dashed lines), however they no longer exhibit a belt-like appearance. The expected inner edges of crescents (dotted lines) are absent in the nonlinear wake, which are in fact shifted outwards beyond the outer edges. For instance, the high density band in Figure 7a near $(x, z)/r_s = (-1.0, 1.5)$ (denoted by "A") tends to fill out the low density region at smaller z/r_p as well as to supply additional material to the outer boundary band at larger z/r_p, achieved only when the perturbation is sufficiently strong (Fig. 7b). The thermal gas pressure close to the crescent's apex ("A") is sufficient in nonlinear regime (Fig. 7b) to spread the material to the point "B" beyond the expected outer boundary. But the flow originated at a lower latitude ("I") is unable to reach the outer edge of the crescent because of the large distance. Instead, it turns back to the inner part, shedding material on the way ("II"), and eventually reaches the edge of the smaller crescent defined in linear regime ("III"). This process raises the density in between the two shock fronts, forming a hill shape of density discontinuity (passing through the point "II").

An extreme nonlinearity is exhibited in Figure 8 for the case of a slower orbital motion ($\mathcal{M}_p =$

2.2) even with a smaller gravitational impact ($r_B/r_p = 0.5$) than in Figure 7b. In fact, the degree of nonlinearity can be defined as $\eta_B = r_B/r_p (\mathcal{M}_p^2 - 1)^{-1}$ for the wake driven by a circularly orbiting object at distance r_p, and the criterion $\eta_B \sim 0.1$ for distinct nonlinear behaviors is found by Kim (2010)[6]. In Figure 8a, the high density region in the orbital plane is not enclosed within the dashed and dotted lines representing the spiral arm boundaries of the corresponding linear wake. Instead, the sharp discontinuity matches the solid line, which is just the inner boundary of the linear counterpart (dotted line) shifted in phase by π. This phase shift is mainly caused by the high pressure at the junction ($r/r_p = \mathcal{M}_p^{-1}$) between the expected outer ($r/r_p = -\varphi\mathcal{M}_p^{-1} + 1$) and inner ($r/r_p = \varphi\mathcal{M}_p^{-1} + 0.2$) boundaries, if the nonlinear effect is ignored, forming a sharp tip. The matter at the tip tends to spread the high density over a larger region due to the steep pressure gradient, unfolding the inner boundary to match the curvature of the outer boundary. This phase shift would be saturated to the maximum value of π in the very nonlinear case, forming a mirror reflecting curve of the inner spiral boundary defined before the nonlinearity is manifested.

The solid curve in Figure 8a can be easily mistaken for a phase shifted outer boundary of a linear wake (e.g., $75°$ for $\mathcal{M}_p = 2$ case in Fig. 3f of Kim 2010) instead of originating from its inner boundary, because the shapes are identical between the two spirals. The π-shifted inner boundary of the linear wake corresponds to the outer boundary of the linear wake shifted by $\pi + 2(\mathcal{M}_p^2 - 1)^{1/2} - \cos^{-1}(2\mathcal{M}_p^{-1} - 1)$, which gives $80°$ in advance for $\mathcal{M}_p = 2.2$. Although it is not clearly seen in the orbital plane, a density discontinuity is found at the location of the outer boundary (defined in the linear counterpart) in Figure 8b for the vertical structure, i.e., the arc structure having x-intercept at $\sim 4r_p$ (see also Fig. 7b). This presence of the expected outer counterpart suggests that the origin of the discontinuity along the solid line is not the outer boundary but it is likely interpreted as the modified inner boundary of the linear wake with the above explanation. As a result, the interior of the nonlinear wake is filled up without a definite inner boundary, except for a moderate interference near the black solid lines in Figure 8b (eq. [10]). The vertical structure of the nonlinear wake is more elliptically shaped than circularly shaped.

As the extension of the solid curve in Figure 8a, the material immediately behind the object also flows over the curved Mach cone shape, advancing $6°.7$ in angle along the orbit. This angle of the isothermal wake ($\gamma = 1$) excellently matches the fit in Kim (2010) for the shock standoff distance in adiabatic gas ($\gamma = 5/3$). It implies that the shock detachment is a common nature of nonlinear flows irrespective of adiabatic index γ as long as the sonic speed is defined as $c_s = (\gamma p/\rho)^{1/2}$. In the process of the overflow creating a new shock front in advance, the flow is highly unstable between the old and new shock fronts, generating low density eddies in extremely nonlinear cases. According to Kim & Kim (2009) for linear trajectory cases, the low density eddies survive only when the detached shock distance from the object in the lateral direction is larger than $r_B\mathcal{M}_p^{-2}$.

---

[6] For rectilinear motion of the object, the similar nonlinear features are characterized by the definition of the degree of nonlinearity with r_p replaced by the gravitational size r_s of the object, $\eta_A = r_B/r_s (\mathcal{M}_p^2 - 1)^{-1}$, and the criterion for nonlinear regime is ~ 2 (Kim & Kim 2009).

It is checked that the lateral distance of the shock in Figure 8a is also larger than this value, corresponding to $0.1r_p$.

Lastly, Figure 8c shows the density enhancement of the wake in this extremely nonlinear regime. The peak values do not have a systematic change from the linear prediction (solid curve), while the minima do not match any of the dashed curves unlike in the linear regime. The minima instead increase to the dotted curve, $\alpha = r_B (r + r_p)^{-1}$, reducing the arm-interarm density contrast in the entire wake. The wake due to circular motion attains a hydrodynamic equilibrium state about the system center. In contrast, the wake due to rectilinear motion has the equilibrium center about the object itself, so that the amplitude of gravitational influence is scaled by r_B/r_s relevant to the object size r_s. The wake of a circularly orbiting object actually tends to achieve quasi-equilibrium about both the object and its orbital center. However, the former influences the localized area at distance from the object of at most $r_B(\mathcal{M}_p^2 - 1)^{-1}$ (if this distance is greater than r_s, and $\mathcal{M}_p > 1$; Kim & Kim 2009; Kim 2010), while the latter affects the wake properties globally. The central value of density enhancement maintains the value of r_B/r_p independent of the nonlinearity, thus readily explaining Kim's (2010) claim that the background density along the orbit is proportional to this value as numerically found $\alpha \approx 0.46(r_B/r_p)^{1.1}$ in equation (10) of Kim (2010).

5. SUMMARY AND DISCUSSION

The formation of a gravitational wake is a characteristic feature of an astronomical object moving through a medium. We examine the wake properties in detail and provide the observable aspects in a quantitative way, by revisiting the previous semianalytic and numerical works (KK07; Kim 2010) and comparing the features with the linear trajectory counterparts discovered in analytic and numerical methods (Ostriker 1999; Kim & Kim 2009).

The analytic formulae for the density wake in the previous work (reviewed in eq. [3] and [4]) do not give a clear physical insight of spiral- and/or arc-shapes. Hence it is difficult to deduce the properties of the wake relevant to the object properties. A further calculation in this paper leads to a purely analytic solution for the wake shape (eq. [5]), which allows detailed description of the wake shape. Simple geometrical approaches are adopted to provide the physical understanding of such shapes. Density enhancement profiles are also investigated. Since the empirical formulae based on the analytic analysis (eq. [11]–[13]) outline the maximum and minimum density enhancement very successfully, these can be directly adopted for interpretation of future simulation and observational data. Our deeper understanding of the linear wake helps to understand nonlinear wakes shown in previous numerical simulations. Particularly, nonlinear aspects such as the increase of background density, the disappearance of inner arm boundary, and the appearance of a detached spiral shock are predictable from a close inspection of linear wake properties.

Considering an object characterized by Bondi accretion radius r_B and circularly orbiting at a distance r_p with an orbital Mach number $\mathcal{M}_p$ in a static uniform gaseous environment, our new

findings for linear wakes are as follows:

1. In the orbital plane of the perturbing object, the linear wake shows excess density in the form of single-armed structure. For supersonic motion, it is confined by distinct boundaries of Archimedes spirals in the form of $r/r_p = \varphi \mathcal{M}_p^{-1} + C$ with different constants C's for the outer (always 1) and the inner (depending on $\mathcal{M}_p$) boundaries. This expression for the explicit form of the spiral shape indicates the pitch angle of $\tan^{-1}(\mathcal{M}_p\, r/r_p)^{-1}$ and the arm spacing of $2\pi r_p \mathcal{M}_p^{-1}$, from which we can deduce the orbital parameters, $\mathcal{M}_p$ and r_p.

2. The vertical structure of the gravitational density wake is quantified for the first time. In meridional planes, the dense regions are bounded by two-centered concentric arcs forming crescent-like structures ($\mathcal{M}_p > 1$), partially overlapping each other for high orbital Mach number ($\mathcal{M}_p > 4.6$) cases. The angular size of the arcs are up to $\lesssim 2 \tan^{-1}(\mathcal{M}_p^2 - 1)^{1/2}$.

3. The density enhancement α at the orbital center is always r_B/r_p.

4. The density enhancement at the edges of the spiral arm pattern can be approximated to $\alpha_{\mathrm{arm}} = \alpha_1 + (4n+2)\,\alpha_{\mathrm{min}}$ with an integer number n depending on $\mathcal{M}_p$ and some definitions of α_1 (eq. [12]) and α_{min} (eq. [11]). The interarm density also increases to $\alpha_{\mathrm{inter}} = (3n-2)\,\alpha_{\mathrm{min}}$ for supersonic cases ($n \geq 1$) and α_{min} for subsonic cases ($n = 0$). Hence the density contrast between arm and interarm regions, $(\rho_{\mathrm{arm}} - \rho_{\mathrm{inter}})/\rho_{\mathrm{inter}} \approx \alpha_{\mathrm{arm}} - \alpha_{\mathrm{inter}}$ in the linear regime ($\alpha_{\mathrm{arm}}, \alpha_{\mathrm{inter}} \ll 1$), is $\sim \alpha_1 + (n+4)\,\alpha_{\mathrm{min}}$ for supersonic cases and $\sim \alpha_1 + \alpha_{\mathrm{min}}$ for subsonic cases. The numerical values for density contrast are approximately r_B/r at large distance ($r \gg r_p$), i.e., $(0.7\text{–}2.9)\,r_B/r$ for a wide range of orbital Mach numbers $\mathcal{M}_p = 0\text{–}0.9$ and $1.5\text{–}10$.

5. The initially static fluid acquires velocity components in an approximate spherical form, starting from near the inner boundaries of high density regions and finally accumulating at the outer boundaries.

6. The gravitational size of the object does not significantly affect the linear wake features insofar as the size is smaller than the interarm gap.

As the accretion capability (r_B/r_p) increases for a marginally supersonic orbital Mach number ($\mathcal{M}_p$), the thermal pressure can be saturated at the junction of high density boundaries appearing as a tip in the linear analysis, so that the inner boundary extends beyond the outer boundary of the pattern. The induced wake reveals the following nonlinear behaviors:

1. An appearance of a detached bow shock and a disappearance of the definite inner arm boundary in the highly nonlinear wake are mutually explained by an overpass of the inner boundary beyond the outer boundary. The shock standoff distance depends only on r_B and $\mathcal{M}_p$, regardless of the adiabatic index γ.

2. Turbulent low density eddies are developed in the unstable process of producing the detached shock via the overpass of the inner boundary beyond the outer boundary. These eddies survive when the shock distance in the lateral direction is larger than $r_B \mathcal{M}_p^{-2}$, consistent to the linear trajectory counterpart in the nonlinear regime.

3. The density enhancement $\alpha = r_B/r_p$ at the orbital center is preserved even in the extremely nonlinear regime, but the interarm density systematically increases proportional to this value, reducing the arm-interarm density contrast.

Using these theoretical diagnostics, we can derive the object mass, velocity, and distance from the orbital center with a given sound speed of the medium. In the case that concentric arcs are observed, the perturbing object is expected to be at the center of the circular arcs, potentially giving r_p. The angular size of the arcs corresponding to $2\tan^{-1}(\mathcal{M}_p^2 - 1)^{1/2}$ probes the orbital Mach number $\mathcal{M}_p$ of the object of interest, or the corresponding velocity V_p with the aid of an estimate of the sound speed c_{s}. The object mass M_p (or the accretion radius $r_B = GM_p/c_{\mathrm{s}}^2$) can be roughly estimated from the density contrast $\sim r_B/r$ at a distance r from the center. High angular resolution observations are required to identify the broadening of arm edges ($\sim 2r_s$) so as to estimate the object size r_s. On the other hand, an observation of a spiral structure can provide information on r_p and $\mathcal{M}_p$ by measurement of arm spacing and arm width. An observation of smooth density distribution without sharp discontinuity provides an upper limit of the object speed ($\mathcal{M}_p < 1$). Finally, an observation of the arm structure with a missing inner boundary suggests the nonlinear wake condition, $r_B/r_p\,(\mathcal{M}_p^2 - 1)^{-1} \gtrsim 0.1$.

From observations of spirals and/or arcs around stars, one may search for the possible existence of unseen companions, which are difficult to be directly detected either due to high obscuration by the dense environment or due to the bright glare of the central object. The presence of the companions may be inferred by their imprints on the environment at large distances from the star. For example, spiral structures have been observed around AB Aur revealed in near-infrared scattered emission (Fukagawa et al. 2004), around AFGL 3068 in dust scattered galactic light (Mauron & Huggins 2006), and around CIT 6 in molecular line emission (Dinh-V.-Trung & Lim 2009).

According to the result in this paper, the density contrast of a gravitational density wake due to a 10 Jupiter mass planet, orbiting at a distance of several AU, is expected to be of the order of 10 % at a distance of a few hundreds AU from the central star, where the spiral arms are located in the circumstellar disk of the Herbig Ae star AB Aur (Fukagawa et al. 2004). Although the density contrast of the order of 10 % is not significant, it may be distinguishable in this disk (rather than spherical) system. Whether such structures can be observed for low mass objects remains to be ascertained. And whether the density contrast due to the gravitational influence of planets has a similar order of magnitude in a disk system also needs to be checked. To clarify the claim of Lin et al. (2006) of forming giant planets as the origin of the observed spiral arms around AB Aur, it is necessary to carefully examine the density profile of the structure.

In the cases of AFGL 3068 and CIT 6, spiral structures are detected on the scale of 1–10 thousand AU (Mauron & Huggins 2006; Dinh-V.-Trung & Lim 2009), which exclude the possibility of planet wakes since the density contrast decreases with distance ($\lesssim 1\,\%$). The large spiral structures in these evolved circumstellar envelopes are likely to be caused by reflex motion of the mass losing star in comparable mass binary system (Soker 1994; Mastrodemos & Morris 1999; He 2007; Edgar et al. 2008). To date, AFGL 3068 is the only object that shows a clear spiral modulation in the circumstellar envelope and its companion star is indeed confirmed by a direct imaging in near-infrared (Morris et al. 2006). The binary separation is about a hundred AU. Recently, Raga et al. (2011) estimated approximately 1 solar mass for the companion of AFGL 3068 from the spiral shape. With this companion mass, the gravitational wake is expected to contribute as much as $100\,\%$ of the envelope density at an observing distance of the wake of a thousand AU, doubling the density in the arm structure. This density contrast of the companion wake may be comparable to the density enhancement due to the reflex motion of the primary star. Hence, in the central region ($\lesssim 1''$ by adopting the distance of $1\,\mathrm{kpc}$ to AFGL 3068), which will be soon resolved by the Atacama Large Millimeter/submillimeter Array (ALMA), there could exist two separated arms caused by two different mechanisms, i.e., one structure due to the reflex motion of the mass losing star and one gravitational density wake of the companion star. A comparison between the two mechanisms is needed in a range of parameter space relevant to the object and background properties.

We note that our analysis is limited to objects in circular motion in a static uniform isothermal gaseous medium. For comparison with detailed observations, our assumptions for the background medium and the object motion may need to be relaxed. However, the wake features described in this paper may suffice to provide a zeroth order approximation of the primary features expected from the gravitational wakes due to such objects.

REFERENCES

Barausse, E. 2007, MNRAS, 382, 826

Barausse, E., & Rezzolla, L. 2008, Phys. Rev. D, 77, 104027

Baruteau, C., Cuadra, J., & Lin, D. N. C. 2011, ApJ, 726, 28

Chavarría, L., Mardones, D., Garay, G., Escala, A., Bronfman, L., & Lizano, S. 2010, ApJ, 710, 583

Conroy, C., & Ostriker, J. P. 2008, ApJ, 681, 151

Dinh-V.-Trung, & Lim, J. 2009, ApJ, 701, 292

Dotti, M., Colpi, M., & Haardt, F. 2006, MNRAS, 367, 103

Dotti, M., Colpi, M., Haardt, F., & Mayer, L. 2007, MNRAS, 369, 956

Edgar, R. G., Nordhaus, J., Blackman, E. G., & Frank, A. 2008, ApJ, 675, L101

El-Zant, A. A., Kim, W.-T., & Kamionkowski, M. 2004, MNRAS, 354, 169

Escala, A., Larson, R. B., Coppi, P. S., & Mardones, D. 2004, ApJ, 607, 765

Escala, A., Larson, R. B., Coppi, P. S., & Mardones, D. 2005, ApJ, 630, 152

Fryxell, B,. Olson, K., Ricker, P., Timmes, F. X., Zingale, M., Lamb, D. Q., MacNeice, P., Rosner, R., Truran, J. W., & Tufo, H. 2000, ApJS, 131, 273

Fukagawa, M., et al. 2004, ApJ, 605, L53

Furlanetto, S. R., & Loeb, A. 2002, ApJ, 565, 854

Garay, G., Mardones, D., Bronfman, L., May, J., Chavarría, L., & Nyman, L.-Å. 2010, ApJ, 710, 567

He, J. H. 2007, A&A, 467, 1081

Jackson, J. D. 1975, Classical Electrodynamics (New York: Wiley)

Just, A., & Kegel, W. H. 1990, A&A, 232, 447

Kim, H., & Kim, W.-T. 2007, ApJ, 665, 432 (KK07)

Kim, H., & Kim, W.-T. 2009, ApJ, 703, 1278

Kim, H., Kim, W.-T., & Sánchez-Salcedo, F. J. 2008, ApJ, 679, L33

Kim, H., & Taam, R. E. 2011, American Institute of Physics Conference Series, 1331, 49 (astro-ph/1012.3469)

Kim, H., & Taam, R. E. 2011, in prep.

Kim, W.-T. 2007, ApJ, 667, L5

Kim, W.-T. 2010, ApJ, 725, 1069

Kim, W.-T., El-Zant, A. A., & Kamionkowski, M. 2005, ApJ, 632, 157

Lin, S.-Y., Ohashi, N., Lim, J., Ho, P. T. P., Fukagawa, M., & Tamura, M. 2006, ApJ, 645, 1297

Mastrodemos, N., & Morris, M. 1999, ApJ, 523, 357

Mauron, N., & Huggins, P. J. 2006, A&A, 452, 257

Mayer, L., Kazantzidis, S., Madau, P., Colpi, M., Quinn, T., & Wadsley, J. 2007, Science, 316, 1874

Morris, M., Sahai, R., Matthews, K., Cheng, J., Lu, J., Claussen, M., & Sánchez-Contreras, C. 2006, Planetary Nebulae in our Galaxy and Beyond, 234, 469

Namouni, F. 2010, MNRAS, 401, 319

Namouni, F. 2011, Ap&SS, 331, 575

Ostriker, E. C. 1999, ApJ, 513, 252

Raga, A. C., Cantó, J., Esquivel, A., Huggins, P. J., & Mauron, N. 2011, Asymmetric Planetary Nebulae 5 Conference, 185

Sánchez-Salcedo, F. J. 2009, MNRAS, 392, 1573

Sánchez-Salcedo, F. J., & Brandenburg, A. 1999, ApJ, 522, L35

Sánchez-Salcedo, F. J., & Brandenburg, A. 2001, MNRAS, 322, 67

Schröder, K.-P., & Connon Smith, R. 2008, MNRAS, 386, 155

Soker, N. 1994, MNRAS, 270, 774

Villaver, E., & Livio, M. 2009, ApJ, 705, L81

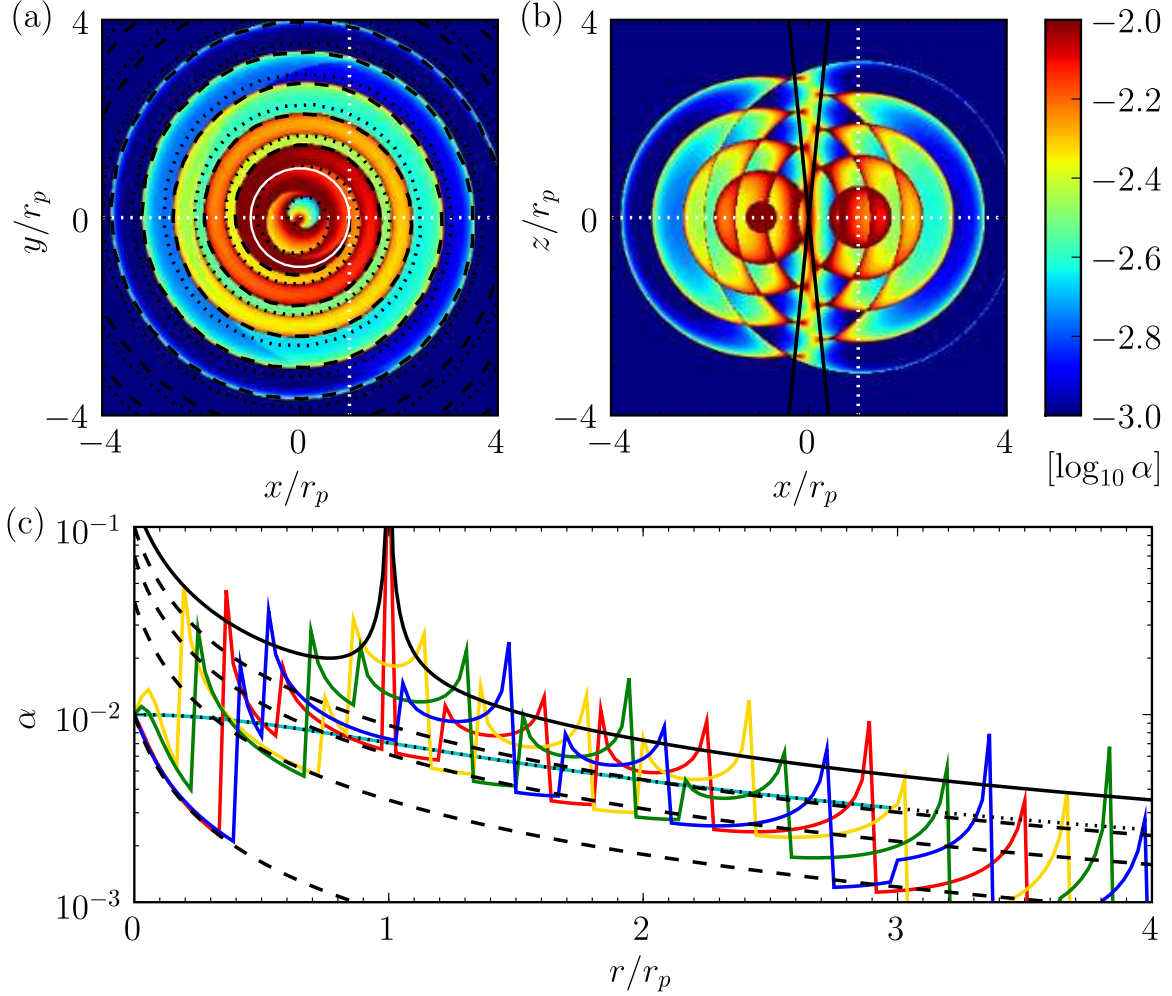Fig. 1.— Density enhancement α of the spiral-onion shell shaped density wake generated by a point mass object orbiting at a fixed distance r_p with an orbital Mach number $\mathcal{M}_p = 10$ in an initially static uniform gaseous medium after 5 orbital periods, calculated by a semianalytic method in KK07. (a) In the orbital plane, the induced density wake possesses a condensed trailing arm bounded by outer (*black dashed*) and inner (*black dotted*) Archimedes spirals $r/r_p = \varphi/\mathcal{M}_p + C$ with $C = 1$ and -0.7, respectively, in the polar coordinates (r, φ) with φ in the clockwise direction tracing the spiral but opposed from the motion of the object. White circle represents the circular orbit of the object, currently located at the intersection of white dotted lines. (b) In a meridional plane, the high density area of the wake displays arcs being able to extend in angle of $\tan^{-1}(\mathcal{M}_p^2 - 1)^{1/2}$ from the orbital plane (*black solid*). White dotted line indicates the current location of the object as in (a). (c) The density enhancement profiles as a function of the distance from the center are displayed along ^+x (*red*), ^-y (*yellow*), ^-x (*green*), ^+y (*blue*), and z (*cyan*) axes. Notice that $\alpha = r_B/r_p$ at the center, where r_B is the Bondi accretion radius of the object. The black solid line ($\alpha = \alpha_1 + 14\alpha_{\min}$) outlines the peaks at the spiral arm boundaries, the dashed lines ($\alpha = \alpha_{\min} \times 1, 4, 7, 10$ from bottom) show the change of minimum density enhancement in the orbital plane because of piling-up of delayed perturbations, and the dotted line represents well the density enhancement of $\alpha_{\min}$ along the orbital axis. See text for more comprehensive explanation including the definition of α_1 and $\alpha_{\min}$.
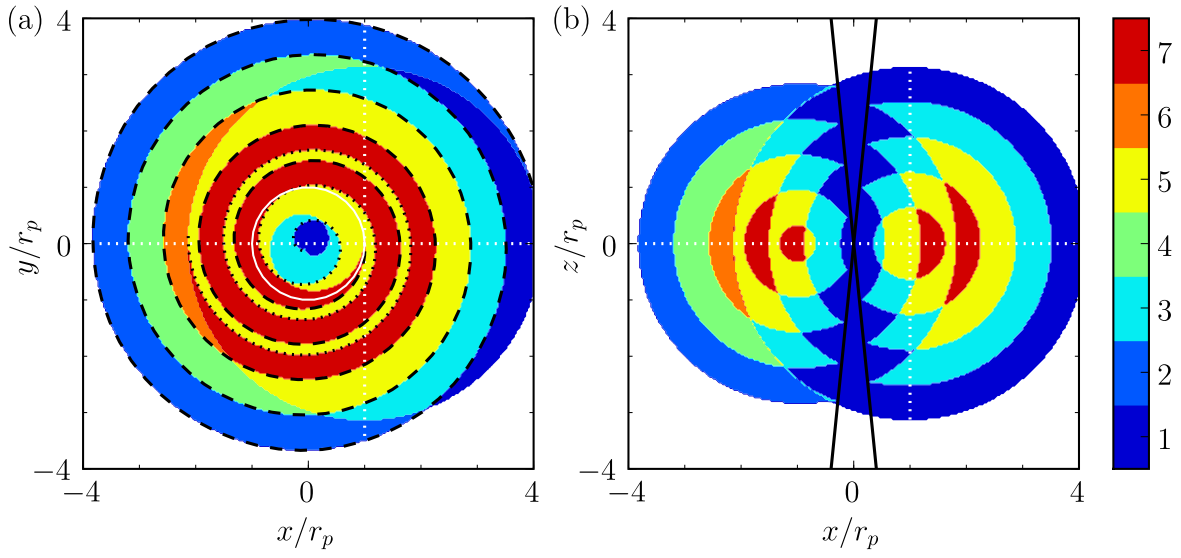
Fig. 2.— Same as Fig. 1a–b, but for the number of perturbations. The perturbing object has circled 5 times with an orbital Mach number of $\mathcal{M}_p = 10$.
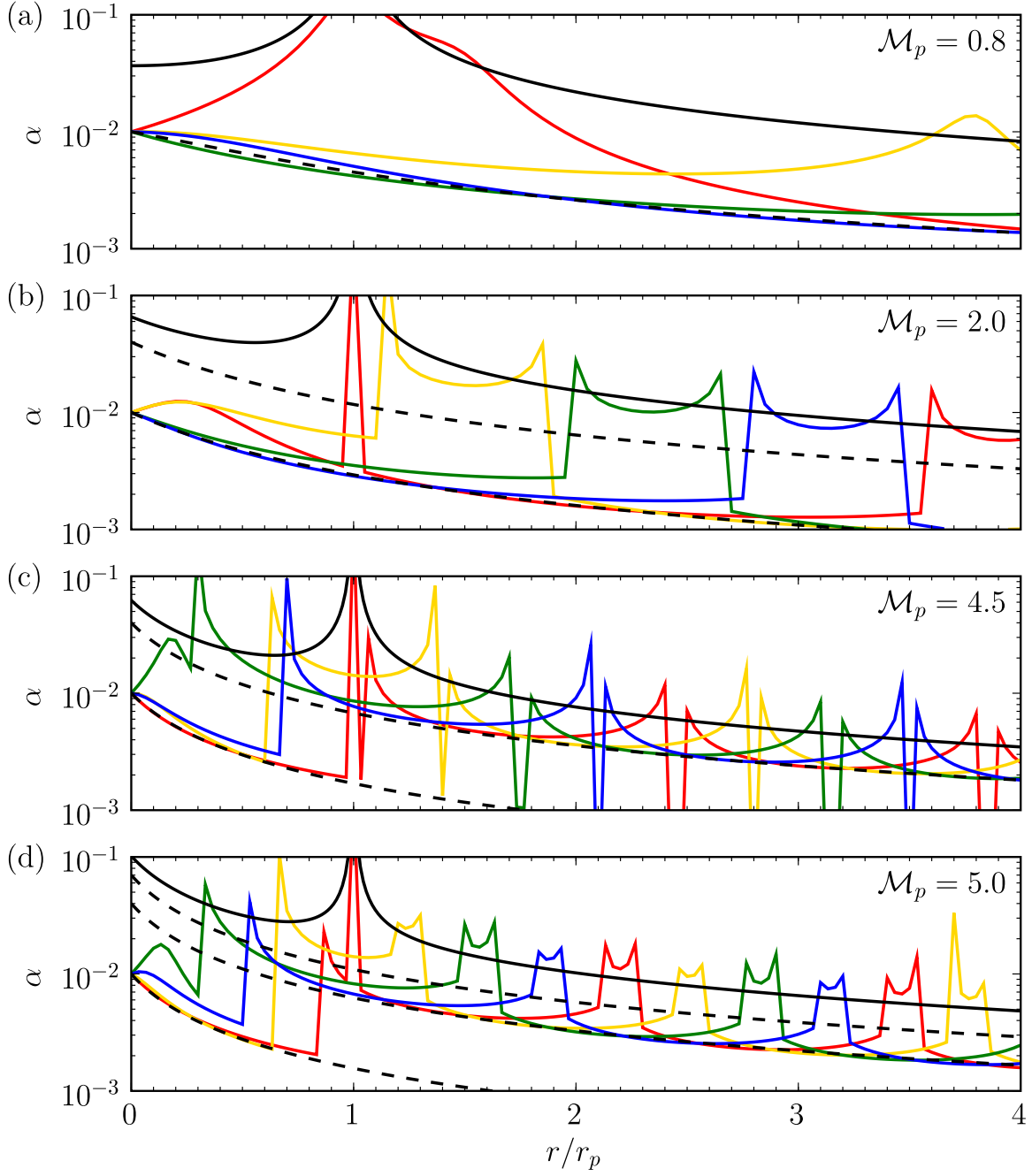
Fig. 3.— Same as Fig. 1c, but for (a) $\mathcal{M}_p = 0.8$ (b) $\mathcal{M}_p = 2.0$, (c) $\mathcal{M}_p = 4.5$, and (d) $\mathcal{M}_p = 5.0$. In each panel, the $n+1$ dashed and one solid lines represent $\alpha = \alpha_{\min} \times 1, 4, \cdots, 1 + 3n$ from bottom and $\alpha = \alpha_1 + (4n + 2)\alpha_{\min}$, respectively, in the orbital plane with n of (a) 0, (b) 1, (c) 1, and (d) 2. See text for the dependence of n on the orbital Mach number $\mathcal{M}_p$, and the definitions of $\alpha_{\min}$ and α_1.
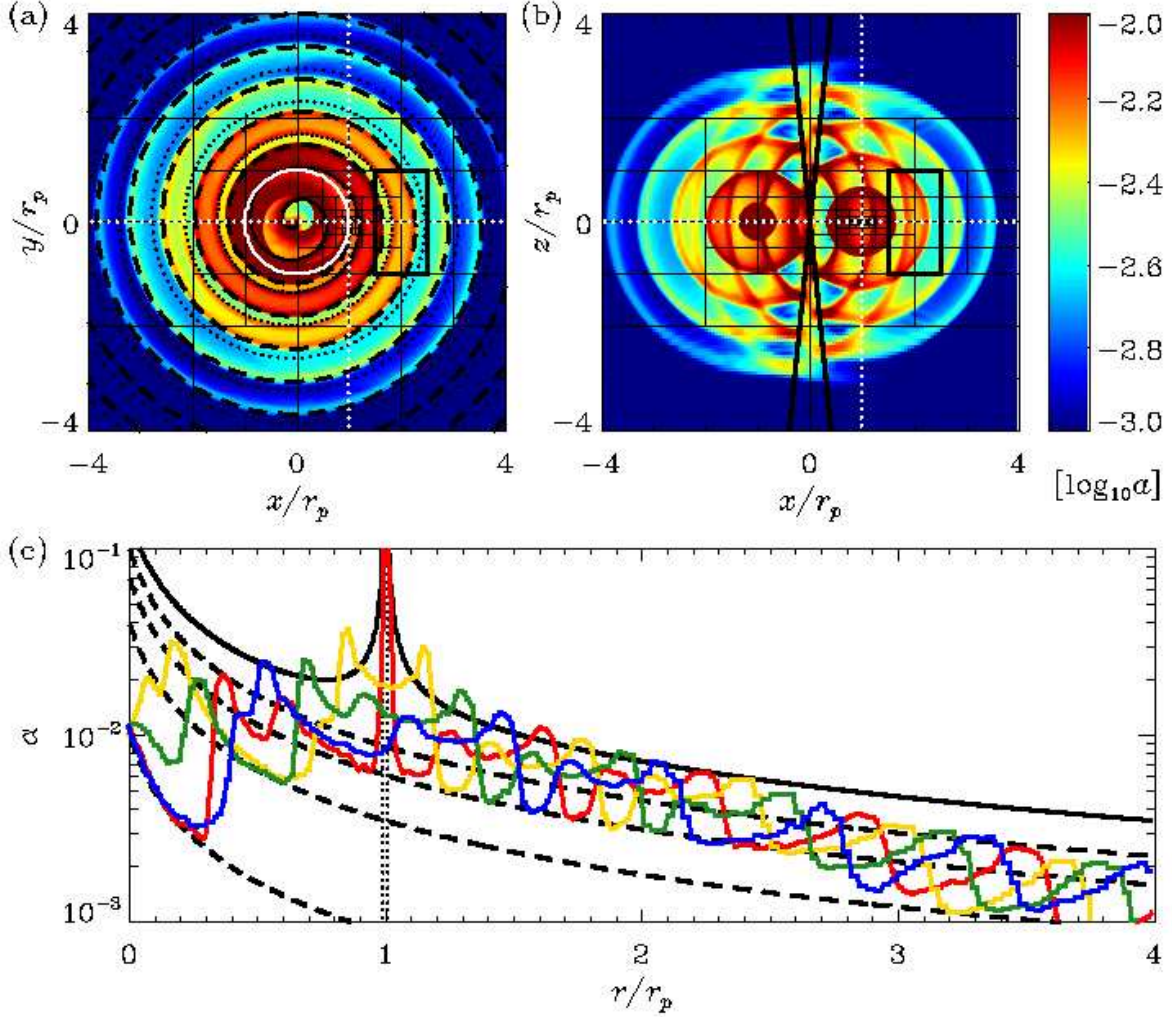
Fig. 4.— Density enhancement α of the spiral-onion shell density wake driven by an extended perturber with the gravitational softening radius of $r_s = 0.01r_p$ in the unit of the orbital radius r_p, calculated by a numerical simulation using an adaptive mesh refinement FLASH code with the maximum refinement level 8 corresponding to the spatial resolution of $0.001r_p$ (as indicated by thin black boxes including $64 \times 64 \times 32$ meshes inside). See Fig. 1 for the details. The thick black boxes in (a) and (b) denote the regions plotted in Fig. 6, and the vertical dotted lines in (c) represent the gravitational size r_s of the object.
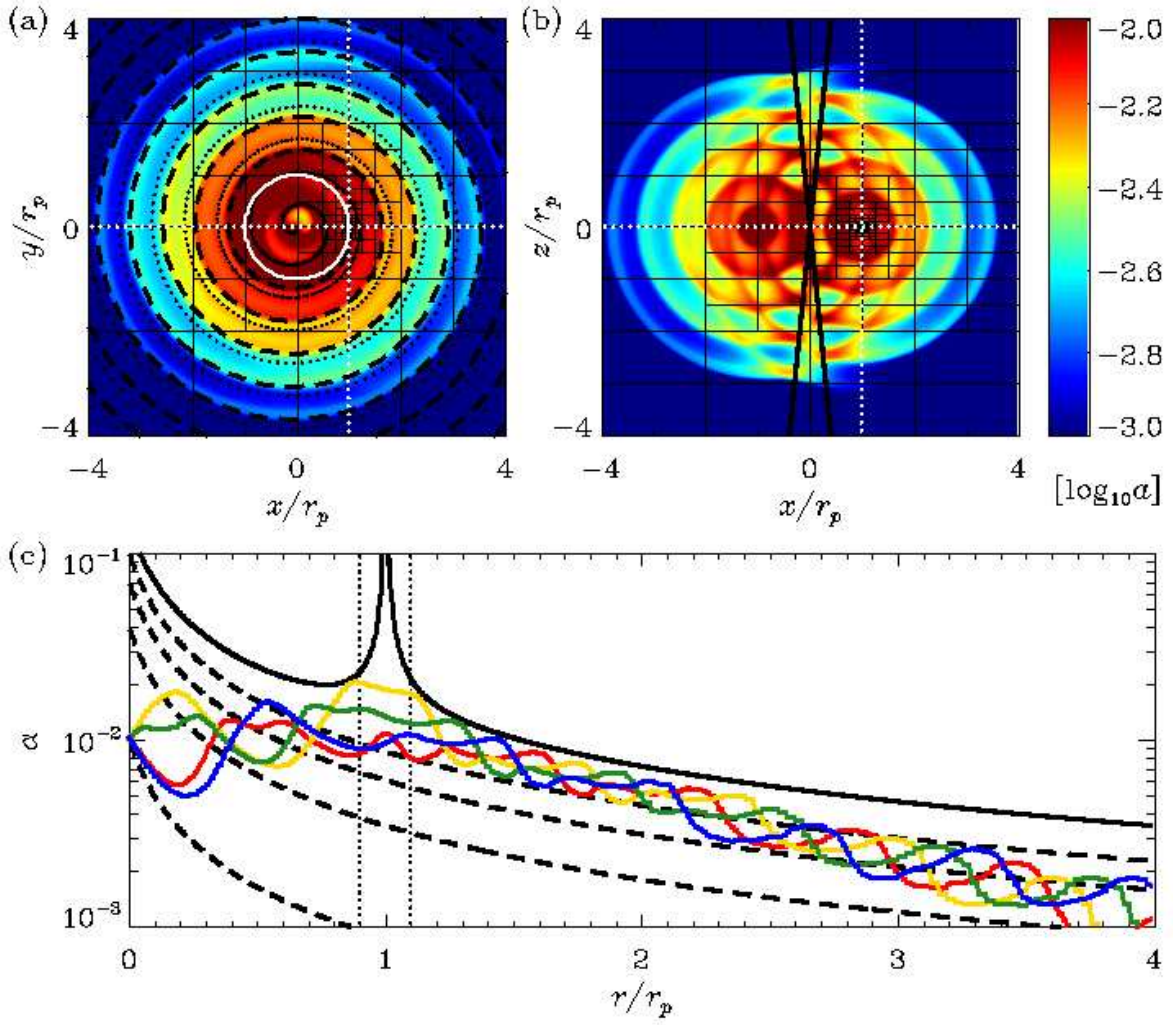
Fig. 5.— Same as Fig. 4, but for a more extended perturber with the gravitational softening radius of $r_s = 0.1r_p$, comparable to half $(0.09r_p)$ of the interarm spacing in the case of a point mass perturber.
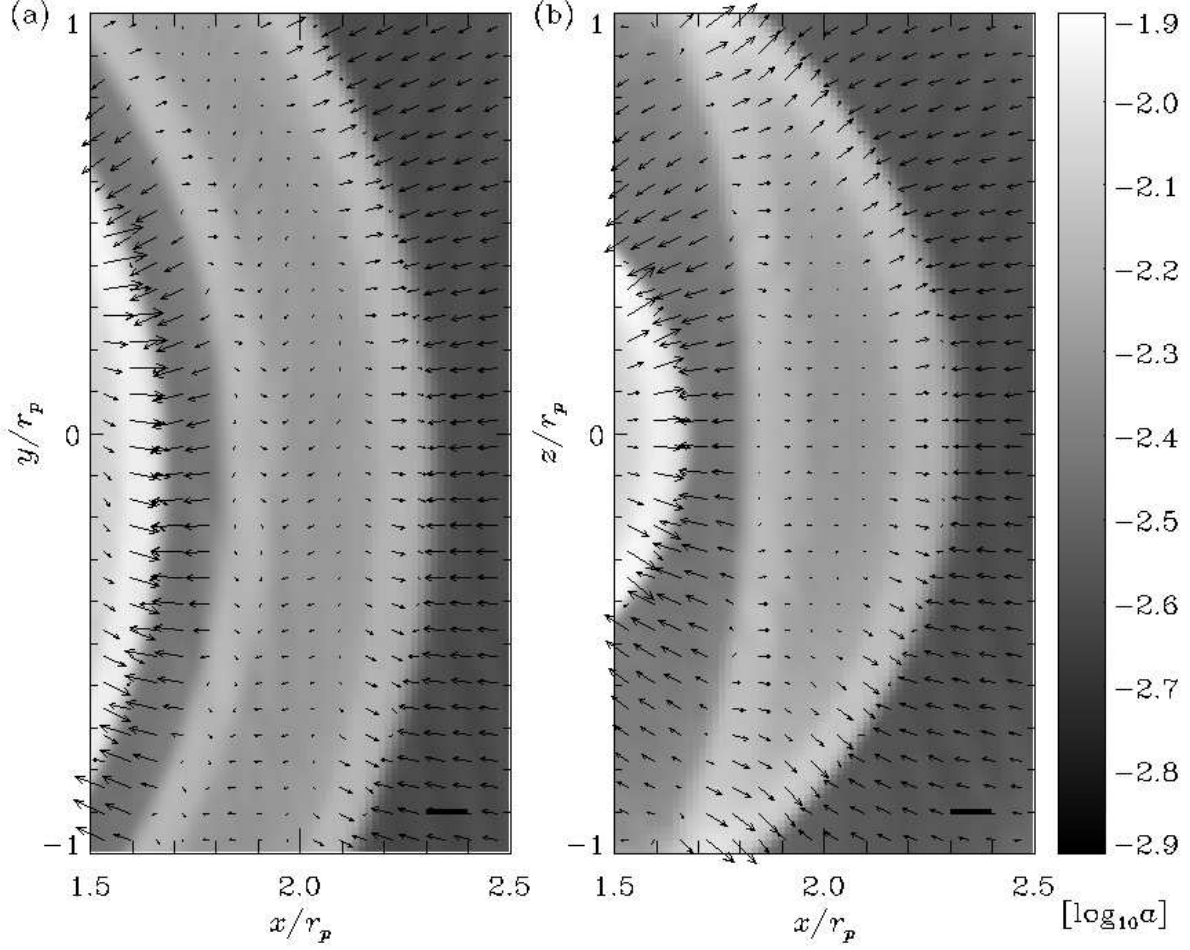
Fig. 6.— Velocity field (arrows) superposed on the map of density enhancement α (logarithmic gray scale) for a segment of high density structure in Fig. 4, observed (a) in the orbital plane ($z = 0$) and (b) in a meridional plane ($y = 0$). The maximum velocity in each panel approximately corresponds to the line segment at the bottom right corner with the magnitude of $\mathcal{M} = r_B \mathcal{M}_p^{-1} |r - r_p|^{-1} \times 2 (r_s/r_p)^{-1/3}$ in Mach number, where r_B, $\mathcal{M}_p$, r_p, and r_s represent the Bondi accretion radius, orbital Mach number, orbital radius, and gravitational size of the perturbing object, respectively, and $r \sim 2r_p$ is adopted.
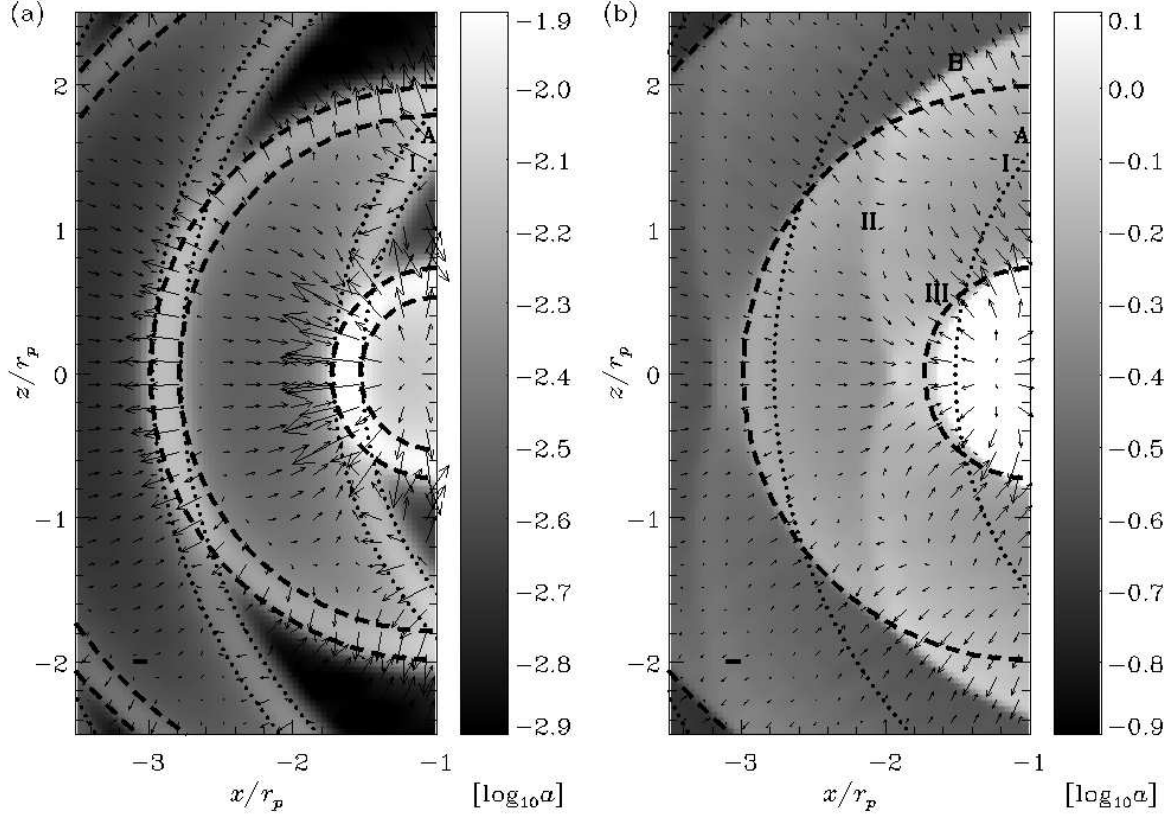
Fig. 7.— Vertical distributions of density enhancement α (logarithmic gray scale) and velocity field (arrows) for the wake created by a gravitational potential characterized by its Bondi accretion radius r_B and softening radius $r_s = 0.1 r_p$, where r_p is the orbital radius of the gravitational object about origin in $z = 0$ plane. The object moving with Mach number $\mathcal{M}_p = 5$ is currently located at $(x, y, z)/r_p = (1, 0, 0)$. (a) Under a weak gravitational potential ($r_B/r_p = 0.01$), the induced wake has the shape of crescents bounded by circular arcs of radii $4\pi\mathcal{M}_p^{-1} + r_s$, $6\pi\mathcal{M}_p^{-1} + r_s$, and $8\pi\mathcal{M}_p^{-1} + r_s$ about the object position with broadening by $\pm r_s$ so as to appear banded (*dotted*) and of radii $1\pi\mathcal{M}_p^{-1}$, $3\pi\mathcal{M}_p^{-1}$, and $5\pi\mathcal{M}_p^{-1}$ about the mirror point from the object with the same broadening (*dashed*). The material flows approximately from inner dotted lines to outer dashed lines. (b) A strong gravitational potential ($r_B/r_p = 1.0$) introduces nonlinear features of the induced wake, different from the corresponding linear wake in (a). For comparison, the inner dotted and outer dashed lines in (a) are copied. Both density and flow speed of nonlinear wake are monotonous compared to those of linear wake. The line segment at bottom left corner represents the fiducial magnitude of velocity vectors in Mach number, $\mathcal{M} = r_B \mathcal{M}_p^{-1} |r - r_p|^{-1} \times 2 \, (r_s/r_p)^{-1/3}$ with adopting $r \sim 2 r_p$. The spatial resolution is $0.04 r_p$ in this area, although the maximum resolution achieved around the object position is twice as high with 5 levels of refinement in FLASH code.
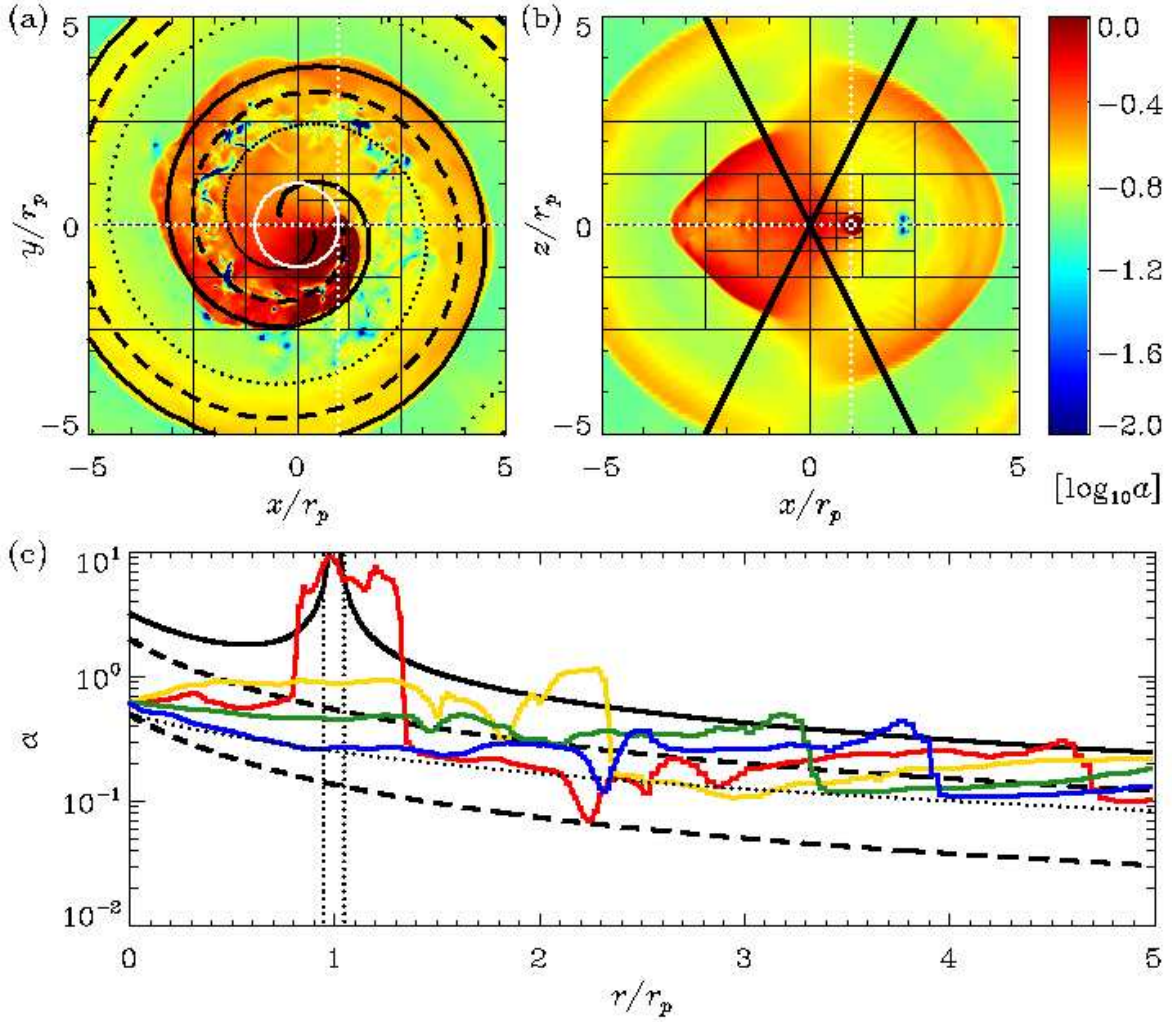
Fig. 8.— Density enhancement α of a nonlinear wake due to a gravitational potential, characterized by the Bondi accretion radius $r_B = 0.5r_p$ and the softening radius $r_s = 0.05r_p$, in circular motion at distance r_p with the Mach number $\mathcal{M}_p = 2.2$. The calculation is performed by FLASH code with the maximum refinement level 5 corresponding to a spatial resolution of $0.01r_p$. (a) In the orbital plane, the nonlinear wake departs in shape from the corresponding linear wake of a single-armed spiral confined in the dashed and dotted curves, but its shock front follows the solid curve, which is the dotted line phase shifted by π. (b) In a meridional plane, the nonlinear wake exhibits the filled elliptical arcs below the solid line as the vertical extension limit of the linear counterpart. (c) The density enhancement profiles along the distance from the center in the orbital plane (colored lines) have the maxima outlined by the black solid line ($\alpha = \alpha_1 + 6\alpha_{\min}$) similarly to the linear counterparts, but the minimum density enhancement follows the dotted line ($\alpha = r_B(r + r_p)^{-1}$) instead of the dashed lines ($\alpha = \alpha_{\min}$ and $4\alpha_{\min}$) for the minimum profiles in linear regime. See text and Fig. 1 for more details.